Temperature effects on adsorption and diffusion dynamics of $CH_3CH_{2(ads)}$ and $H_3C–C{\equiv}C_{(ads)}$ on Ag(111) surface and their self-coupling reactions: *Ab initio* molecular dynamics approach

Shao-Yu Lu and Jyh-Shing Lin[a)]
Department of Chemistry, Tamkang University, Tamsui 25137, Taiwan

(Received 6 September 2013; accepted 18 December 2013; published online 13 January 2014)

Density functional theory (DFT)-based molecular dynamics (DFTMD) simulations in combination with a Fourier transform of dipole moment autocorrelation function are performed to investigate the adsorption dynamics and the reaction mechanisms of self-coupling reactions of both acetylide ($H_3C–C_{(\beta)}{\equiv}C_{(\alpha)\,(ads)}$) and ethyl ($H_3C_{(\beta)}–C_{(\alpha)}H_{2(ads)}$) with $I_{(ads)}$ coadsorbed on the Ag(111) surface at various temperatures. In addition, the calculated infrared spectra of $H_3C–C_{(\beta)}{\equiv}C_{(\alpha)(ads)}$ and I coadsorbed on the Ag(111) surface indicate that the active peaks of $–C_{(\beta)}{\equiv}C_{(\alpha)}–$ stretching are gradually merged into one peak as a result of the dominant motion of the stand-up $–C–C_{(\beta)}{\equiv}C_{(\alpha)}–$ axis as the temperature increases from 200 K to 400 K. However, the calculated infrared spectra of $H_3C_{(\beta)}–C_{(\alpha)}H_{2(ads)}$ and I coadsorbed on the Ag(111) surface indicate that all the active peaks are not altered as the temperature increases from 100 K to 150 K because only one orientation of $H_3C_{(\beta)}–C_{(\alpha)}H_{2(ads)}$ adsorbed on the Ag(111) surface has been observed. These calculated IR spectra are in a good agreement with experimental reflection absorption infrared spectroscopy results. Furthermore, the dynamics behaviors of $H_3C–C_{(\beta)}{\equiv}C_{(\alpha)(ads)}$ and I coadsorbed on the Ag(111) surface point out the less diffusive ability of $H_3C–C_{(\beta)}{\equiv}C_{(\alpha)(ads)}$ due to the increasing *s*-character of C_α leading to the stronger $Ag–C_\alpha$ bond in comparison with that of $H_3C_{(\beta)}–C_{(\alpha)}H_{2(ads)}$ and I coadsorbed on the same surface. Finally, these DFTMD simulation results allow us to predict the energetically more favourable reaction pathways for self-coupling of both $H_3C–C_{(\beta)}{\equiv}C_{(\alpha)(ads)}$ and $H_3C_{(\beta)}–C_{(\alpha)}H_{2(ads)}$ adsorbed on the Ag(111) surface to form 2,4-hexadiyne ($H_3C–C{\equiv}C–C{\equiv}C–CH_{3(g)}$) and butane ($CH_3–CH_2–CH_2–CH_{3(g)}$), respectively. The calculated reaction energy barriers for both $H_3C–C{\equiv}C–C{\equiv}C–CH_{3(g)}$ (1.34 eV) and $CH_3–CH_2–CH_2–CH_{3(g)}$ (0.60 eV) are further employed with the Redhead analysis to estimate the desorption temperatures approximately at 510 K and 230 K, respectively, which are in a good agreement with the experimental low-coverage temperature programmed reaction spectroscopy measurements.
 [http://dx.doi.org/10.1063/1.4861036]

I. INTRODUCTION

The study of carbon-carbon bond formation at metal surfaces is of great importance for understanding the nature of the chemical reactions involved in heterogeneous catalytic processes. Specifically, the self-coupling of alkyls (C_nH_{2n+1}),[1–3] carbenes (C_nH_{2n}),[4,5] and carbynes (C_nH_{2n-1})[6,7] to form the long-chain hydrocarbons through the famous Fischer-Tropsch[8] (FT) synthesis has been established on a number of transition metal surfaces. The detailed adsorbed structures, their orientations, and their corresponding reaction mechanisms were usually explored by reflection absorption infrared spectroscopy (RAIRS), electron energy loss spectroscopy (EELS), surface enhanced Raman spectroscopy (SERS), and temperature programmed reaction spectroscopy (TPRS).[9,10] Over the past few decades, several research works have been devoted to the study of self-coupling reaction of hydrocarbons adsorbed on the Ag(111) surface. For example, Chiang's research group illustrated the self-coupling reaction for acetylide ($H_3C–C_{(\beta)}{\equiv}C_{(\alpha)(ads)}$) adsorbed on the Ag(111) surface by using TPRS and RAIRS.[11] Their experimental results suggested that $H_3C–C_{(\beta)}{\equiv}C_{(\alpha)(ads)}$ adsorbed on the Ag(111) surface will self-couple to form $H_3C–C{\equiv}C–C{\equiv}C–CH_{3(g)}$ approximately at 500 K. In addition, Zhou and White also employed the same strategy to investigate the reaction temperature for self-coupling reaction of adsorbed ethyl ($H_3C_{(\beta)}–C_{(\alpha)}H_{2(ads)}$) and vinyl ($H_2C_{(\beta)}{=}C_{(\alpha)}H_{(ads)}$) on the Ag(111) surface, which were found approximately at 200 K and 250 K,[12,13] respectively. These results suggest that the reaction rates of the $C_\alpha–C_\alpha$ (tail-to-tail dimerization) self-coupling are in the order of $C_{sp3}–C_{sp3} > C_{sp2}–C_{sp2} \gg C_{sp}–C_{sp}$. To rationalize the nature of the metal-substrate interaction involved in self-coupling reactions as mentioned above, Weaver and co-workers investigated both ethylene ($H_2C{=}CH_{2(ads)}$) and ethylidyne ($H_3C{\equiv}C_{(ads)}$) adsorbed on platinum-group and coinage-metal (Cu, Ag, Au) by using EELS and SERS[14] and realized that the increasing of the binding energy of $M\text{-}C_\alpha$ is correlated with the increasing s-character of the hybridization state of C_α. Their experimental results proposed that the reverse order for the $M\text{-}C_\alpha$ bond strength $M\text{-}C_{sp} > M\text{-}C_{sp2} \gg M\text{-}C_{sp3}$ is due to the back donation of the occupied *d*-bands of the metal surface to the C_α

a)Author to whom correspondence should be addressed. Electronic mail: jsl@mail.tku.edu.tw

anti-bonding orbitals (σ^* and π^*).[15,16] Finally, these experimental results lead to the conclusion that the strongest bond of M-C_α may render the slowest rate of C_α–C_α self-coupling reactions.

To provide more insight into the reaction mechanisms of C_α–C_α self-coupling of different hydrocarbons adsorbed on metal surface, White employed temperature-dependent RAIRS in combination with TPRS to investigate the reaction mechanisms of both ethyl ($H_3C_{(\beta)}$–$C_{(\alpha)}H_{2(ads)}$) and 2,2,2-Trifluoroethyl ($CF_3CH_{2(ads)}$) adsorbed on the Ag(111) surface.[17] Their temperature-dependent RAIRS results proposed the possible geometries of adsorbed structures, including their orientations of both $H_3C_{(\beta)}$–$C_{(\alpha)}H_{2(ads)}$ and $CF_3CH_{2(ads)}$ adsorbed on the Ag(111) surface at various temperatures. Moreover, their TPRS results elucidated that the stronger molecule-surface interaction might block the migratory self-coupling reaction of $CF_3CH_{2(ads)}$ adsorbed on the Ag(111) surface leading to the lower coupling reaction rate. Another factor to affect the long-chain growth is the hydrogenation reaction of hydrocarbons. The hydrogenation reaction of unsaturated hydrocarbons is usually a first possible step during the FT synthesis. Both experimental and theoretical groups devote themselves to try to thoroughly understand the whole reaction mechanisms for the long-chain growth in FT synthesis. Huand Liu *et al.* provide a series of the state of art DFT calculations to investigate the complete microscopic picture of elementary steps for C_1 and C_2 related hydrocarbon species on several metal surfaces in FT synthesis.[18–20] Their calculated results show that the direct self-coupling reactions have a much lower reaction barrier than the hydrogenation reactions on Ru surfaces. However, the competition between self-coupling reaction and hydrogenation reaction of hydrocarbons has also been carried out in Chiang's TPR/D experiments. They found that the hydrogenation of H_3C–$C_{(\beta)}\equiv C_{(\alpha)(ads)}$ adsorbed on the Ag(111) surface is at 470 K, which is at the same temperature as the direct self-coupling reaction. Besides, the most product yield of m/z ($C_6H_6^+$) species is validated to be 2,4-hexiadine (H_3C–C≡C–C≡C–$CH_{3(g)}$). Therefore, the hydrogenation reaction of H_3C–$C_{(\beta)}\equiv C_{(\alpha)(ads)}$ can be neglected and we only focus on the issue of the self-coupling of hydrocarbon to study the effect of different hybridization state of C_α atom for direct C–C self-coupling reaction. Additionally, the intermediate geometries along the self-coupling reactions are difficult to measure and the electronic properties for metal-carbon bond still remain unclear followed by their experimental results. Hence, it is necessary to employ the density functional theory-based molecular dynamics (DFTMD) simulations in order to investigate the influence of temperature on the dynamic behaviors of different hydrocarbons adsorbed on metal surfaces. In particular, the simulated vibrational spectroscopy has been widely used to probe their intermediate structures and their adsorption dynamics of molecules absorbed on the metal surfaces, and much more progress has been reported regarding the elementary steps of chemical reactions on metal surface, including CO oxidative reaction,[21] oxygen adsorption,[22] water adsorption,[23–25] and hydrogen adsorption on metal surfaces[26] based on first principle molecular dynamic simulations. Followed by these pioneer's works, our research group also carried out the DFTMD simulations in combination with a Fourier transform of dipole moment autocorrelation (FT-DMAF) to investigate the effect of temperature on vibrational modes of H_3C–$C_{(\beta)}\equiv C_{(\alpha)(ads)}$ and I coadsorbed on the Ag(111) surface[27] and pointed out that the increased flipping from the titled motion of –C–$C_{(\beta)}\equiv C_{(\alpha)}$– axis to the stand-up motion of –C–$C_{(\beta)}\equiv C_{(\alpha)}$– axis followed by its diffusion resulting from the increasing temperature from 200 K to 400 K seems to be the initial event to initiate the alkyne self-coupling reaction. Indeed, our simulated results of H_3C–$C_{(\beta)}\equiv C_{(\alpha)(ads)}$ adsorbed on the Ag(111) surface clearly provide insight into the understanding of adsorption behaviors. But the detailed reaction mechanism of C_α–C_α self-coupling and their corresponding nature of metal-carbon interaction still remain unanswered.

Therefore, in this paper, we will first calculate adsorption geometries and electronic structures of ethyl ($H_3C_{(\beta)}$–$C_{(\alpha)}H_{2(ads)}$) and acetylide (H_3C–$C_{(\beta)}\equiv C_{(\alpha)(ads)}$) with iodine ($I_{(ads)}$) coadsorbed on Ag(111) surface in order to realize their bonding nature of Ag–C_α interaction. Then we will employ DFTMD simulations to investigate the effect of temperature on the adsorption dynamics of both ethyl ($H_3C_{(\beta)}$–$C_{(\alpha)}H_{2(ads)}$) and acetylide (H_3C–$C_{(\beta)}\equiv C_{(\alpha)(ads)}$) with $I_{(ads)}$ coadsorbed on the Ag(111) surface. As a byproduct, based on a FT-DMAF, the simulated temperature-dependent IR spectra can help identify the structures of both $H_3C_{(\beta)}$–$C_{(\alpha)}H_{2(ads)}$ and H_3C–$C_{(\beta)}\equiv C_{(\alpha)(ads)}$ adsorbed on the Ag(111) surface. Finally, the collected trajectories of both $H_3C_{(\beta)}$–$C_{(\alpha)}H_{2(ads)}$ and H_3C–$C_{(\beta)}\equiv C_{(\alpha)(ads)}$ during DFTMD simulations at various temperatures allow us to predict the thermally most favorable reaction pathways for self-coupling reaction of $H_3C_{(\beta)}$–$C_{(\alpha)}H_{2(ads)}$ and H_3C–$C_{(\beta)}\equiv C_{(\alpha)(ads)}$ adsorbed on the Ag(111) surface to form 2,4-hexadiyne (H_3C–C≡C–C≡C–$CH_{3(g)}$) and butane (CH_3–CH_2–CH_2–$CH_{3(g)}$), respectively.

II. COMPUTATIONAL METHODS

The calculations of possible structural models of $H_3C_{(\beta)}$–$C_{(\alpha)}H_{2(ads)}$ and H_3C–$C_{(\beta)}\equiv C_{(\alpha)(ads)}$ with $I_{(ads)}$ coadsorbed on the Ag(111) surface are performed using SIESTA,[28] a DFT-based code with Troullier-Martins norm-conserving pseudopotentials.[29] The spin-polarized version of the generalized gradient approximation (GGA) according to Perdew-Burke-Ernzerhof (PBE)[30] is used for the exchange-correlation function. A split valence double-ζ atomic orbital plus a polarization orbital are chosen as basis sets for all of the atoms. The localization radii of basis functions are determined from an energy cutoff of 0.01 Ry. The Kohn-sham orbitals are expanded in a localized basis set (double-ζ) with the mesh cutoff of 150 Ry. Both energy cutoff and mesh cutoff parameters are chosen after convergence tests, which were described in our previous works.[27] The Ag(111) surface is represented by a Ag(111)-4×4 surface model and is constructed by a periodically repeated three-layer slab of Ag atoms, in which the bottom 2 layers are fixed and the topmost layer is relaxed with a vacuum region of ∼16 Å.[31] For the Brillouin-zone integration, a (3 × 3 × 1) grid determined by Monkhorst-Pack special points is used.[32] In addition, the basis set superposition error (BSSE) has been considered in all of the

calculated adsorption energies of both $H_3C_{(\beta)}$–$C_{(\alpha)}H_{2(ads)}$ and H_3C–$C_{(\beta)}\equiv C_{(\alpha)(ads)}$ with $I_{(ads)}$ coadsorbed on the Ag(111) surface using the counterpoise correction. In order to obtain the partial density of states (PDOS), the total density of states (TDOS) of the whole system is first generated and then the TDOS is decomposed into the contribution of partial fragments, that is, the adsorbed molecule and the surface layer atoms of those selected bands to give rise to the PDOS. In this study, the C_α of the adsorbed molecules and their neighboring Ag surface atoms are considered as the constituent atoms to generate the PDOS. The energy width for broadening the eigenvalues is 0.2 eV.

To investigate the adsorption dynamics of both $H_3C_{(\beta)}$–$C_{(\alpha)}H_{2(ads)}$ and H_3C–$C_{(\beta)}\equiv C_{(\alpha)(ads)}$ with $I_{(ads)}$ coadsorbed on the Ag(111) surface at various temperatures, the molecular dynamics simulations based on DFTMD[33] are performed using the same program, SIESTA. To reduce the computational cost the Ag(111) surface is represented by a Ag(111)-3×3 surface model and is constructed by a periodically repeated slab of Ag atoms with three layers, in which the topmost layer is allowed to relax. The vacuum region is set to be ∼16 Å. All of the simulations are performed in the *NVT* ensemble using Nose-Hoover thermostats.[34,35] The first part of DFTMD simulation is to reach an equilibration phase with a time step of 0.5 fs for at least 1.0 ps. Then, the second part of the simulation, which lasts for 8.0 ps, is followed by collecting data over the temperature-controlled dynamic trajectory to generate the time-dependent autocorrelation of the physical properties of interest.

Taking the surface dipole selection rule into account, the IR spectrum is generated from the time-dependent dipole moment ($\mu(t)_{DM}$) relative to any arbitrary dipole moment ($\mu(0)_{DM}$) of any adsorbed systems based on the temperature-controlled dynamic trajectory of the DFTMD simulation mentioned above. To achieve this goal, the dipole moment autocorrelation function (DMAF), that is, $C^z(t)_{DMAF}$, is constructed as follows:

$$C^z(t)_{\mathrm{DMAF}} = \langle \mu^z(0)_{\mathrm{DM}} \mu^z(t)_{\mathrm{DM}} \rangle.$$

One point worth mentioning is the way that the dipole moments of both $H_3C_{(\beta)}$–$C_{(\alpha)}H_{2(ads)}$ and H_3C–$C_{(\beta)}\equiv C_{(\alpha)(ads)}$ with $I_{(ads)}$ coadsorbed on the Ag(111) surface are calculated ; Followed by the same reason mentioned in our previous paper.[27] The "full DFT Grid charge method" is introduced as follows:

$$\mu^z(t)_{DM} = \sum_i^N q_i(t) \vec{r_i^z}(t),$$

where q_i (t) are calculated DFT grid charges at each time step and N is the total number of grids. Due to the surface selection rule, only the z component (perpendicular to the surface) of position vector of grid i at each time step ($\vec{r_i^z}$(t)) was used to calculate the dipole moment, which includes both the metal surface and the adsorbates. The IR spectrum, namely, $C^z(\omega)$, is then calculated by a Fourier transform of $C^z(t)_{DMAF}$ as follows:

$$C^z(\omega)_{\mathrm{FT-DMAF}} = \frac{2\pi\beta\omega^2}{3cV} \int_{-\infty}^{\infty} C^z(t)_{\mathrm{DMAF}} dt e^{i\omega t},$$

where β is equal to $1/k_BT$, in which k_B is Boltzman's constant and T is the temperature. In addition, ω is the frequency, ν is the volume, and c is the speed of the light.[36,37] In order to enhance the signal-to-noise ratio of adsorption systems, a sufficient simulation time for sampling is required. As mentioned earlier the total simulation time of 8 ps is employed for all DFTMD simulations. As a result, a nearly 4 cm^{-1} spectral resolution is achieved based on a discrete Fourier transform of calculated DMAF followed by smoothing the peaks with Lorentzian functions.

To investigate how the effect of temperature on the dynamic motions of vibrational modes of both $H_3C_{(\beta)}$–$C_{(\alpha)}H_{2(ads)}$ and H_3C–$C_{(\beta)}\equiv C_{(\alpha)(ads)}$ adsorbed on the Ag(111) surface, the temperature-difference spectrum[38] is applied in this work. Followed the DFTMD simulation results, the IR spectrum associated with the two different temperatures is also calculated. Then the temperature-difference spectrum is generated as the following equation:

$$C^z_{\mathrm{difference}}(\omega) = C^z(\omega)_{\mathrm{FT-DMAT-T1}} - C^z(\omega)_{\mathrm{FT-DMAT-T2}}.$$

Finally, following the adsorption dynamics of both $H_3C_{(\beta)}$–$C_{(\alpha)}H_{2(ads)}$ and H_3C–$C_{(\beta)}\equiv C_{(\alpha)(ads)}$ adsorbed on the Ag(111) surface at various temperatures, it is possible to predict the most thermally favorable reaction pathways for self-coupling reaction. The transition states are searched using partial structural constraint path minimization (PSCPM) method[39,40] in order to calculate their corresponding activation energies. A minima structure (no imaginary frequency) and a transition state (one and only one imaginary normal mode frequency) are verified. The calculated activation energies for the corresponding elementary reactions are corrected by the zero-point vibrational energies (ZPE). In addition, *Polanyi-Wigner* equation[41,42] and Redhead Approximation[43] are employed in order to obtain the reaction temperature for self-coupling reaction. The process of desorption, based on this approximation, can be described by the *Polanyi-Wigner* equation, which is derived from Arrhenius-type behavior as the following:

$$r_{des} = -\frac{dN}{dt} = \upsilon N^x exp\left(-\frac{\Delta E}{RT}\right).$$

Here, N is the surface concentration (coverage), t is the reaction time, x is the reaction order, υ is the frequency factor, ΔE is the activation energy of the desorption process, and T is the reaction temperature. In TPRS experiment, the number of desorbing molecules (I) is proportional to the rate of desorption. In addition, the process of desorption is accompanied with a heating rate $_\beta$. Then, the time t is substituted into the *Polanyi-Wigner* equation by dt = $(1/_\beta)$dT:

$$\mathrm{I(T)} \propto r_{des} = -\frac{dN}{dT} = \frac{\upsilon N^x}{\beta} \exp\left(-\frac{\Delta E}{RT}\right).$$

The *Polanyi-Wigner* equation is solved to find the temperature (T_{max}) at which the desorption rate is a maximum leading to the following equation:

$$\frac{\Delta E}{RT_{max}^2} = \frac{\upsilon x N^{x-1}}{\beta} \exp\left(-\frac{\Delta E}{RT_{max}}\right).$$

For a second-order self-coupling reaction, the T_{max} depends on the surface coverage N. The *Polanyi-Wigner* equation can

TABLE I. Calculated adsorption energies (E_{ads}) and corresponding structural parameters of both H_3C–$C_{(\beta)}{\equiv}C_{(\alpha)(ads)}$ and $H_3C_{(\beta)}$–$C_{(\alpha)}H_{2(ads)}$ with $I_{(ads)}$ bonded to the threefold hollow site on the Ag(111) surface.

Model	Site	E_{ads} (eV)	hAg⊥C_α (Å)	$dC_\alpha C_{\beta\backslash}$ (Å)
$H_3CC{\equiv}C_{(ads)}$ and $I_{(ads)}$ co-adsorbed on Ag(111)		C_α-position		$C_\alpha{\equiv}C_\beta$
	Top	−5.54	1.925	1.250
	Bridge	−6.08	1.612	1.249
	FccH	−6.20	1.613	1.249
	HcpH(standup)	−6.47	1.482	1.251
	HcpH(tilted)	−6.53	1.411	1.264
$CH_3CH_{2(ads)}$ and $I_{(ads)}$ co-adsorbed on Ag(111)		C_α-position		C_α–C_β
	Top	−3.55	2.152	1.521
	Bridge	−3.28	2.098	1.534
	FccH	−3.39	2.089	1.535
	HcpH	−3.25	2.085	1.534

be rewritten by x = 2 as the following:

$$\frac{\Delta E}{RT_{max}} = \ln\left(\frac{2\upsilon NT}{\beta}\right) - \ln\left(\frac{\Delta E}{RT_{max}}\right).$$

According to Redhead's approximation, the second part in brackets is quite small relative to the first part and is estimated as $ln(\Delta E/RT_{max}) = 3.64$. The error introduced through this estimate is less than 1.5% for $10^8 < \upsilon / \beta < 10^{13}$ K^{-1}. Hence, the activation energies for self-coupling reaction can be converted into the reaction temperature. The choice of appropriate energy barrier for representing the reaction temperature along the reaction pathway will be discussed in the Results and Discussion section.

III. RESULTS AND DISCUSSION

A. Structural and electronic properties of both $H_3C_{(\beta)}C_{(\alpha)}H_2I_{(ads)}$ and H_3C–$C_{(\beta)}{\equiv}C_{(\alpha)}$–$I_{(ads)}$ adsorbed on the Ag(111) after C–I bond scission

Due to the very weak C–I bond, the C–I cleavage within both $H_3C_{(\beta)}C_{(\alpha)}H_2I_{(ads)}$ and H_3C–$C_{(\beta)}{\equiv}C_{(\alpha)}$–$I_{(ads)}$ adsorbed on the Ag(111) surface occur at 110-K and 150-K, respectively, which were found by White's and Chiang's experimental works. Recently, our research group systematically investigated the reaction mechanism of the C–I cleavage within H_3C–$C_{(\beta)}{\equiv}C_{(\alpha)}$–$I_{(ads)}$ adsorbed on the Ag(111) surface by using DFT calculations. Following the adsorption behavior of H_3C–$C_{(\beta)}{\equiv}C_{(\alpha)(ads)}$ and $I_{(ads)}$ coadsorbed on the Ag(111) surface after the rupture of C–I bond, $I_{(ads)}$ is found to be energetically more favorable to locate on the threefold hollow site. In addition, two most stable adsorption structures out of five possible adsorption structural models of H_3C–$C_{(\beta)}{\equiv}C_{(\alpha)(ads)}$ and $I_{(ads)}$ coadsorbed on the Ag(111) surface are determined. The adsorption energies and structural parameters are summarized in Table I and their corresponding optimized structures are shown in Figure 1. First, the adsorbed H_3C–$C_{(\beta)}{\equiv}C_{(\alpha)(ads)}$ is located on hcpH site and the –$C_\beta{\equiv}C_\alpha$– axis is aligned horizontal to the Ag surface with the adsorption energy of −6.53 eV, namely, the H_3C–$C_{(\beta)}{\equiv}C_{(\alpha)(ads)}$(hcp-tilted)$_{(ads)}$. Second, the adsorbed H_3C–$C_{(\beta)}{\equiv}C_{(\alpha)(ads)}$ is located on the hcpH site and the $-C_\beta{\equiv}C_\alpha-$ axis is aligned perpendicular to the Ag surface with slightly higher adsorption energy of −6.47 eV, namely, the H_3C–$C_{(\beta)}{\equiv}C_{(\alpha)(ads)}$ (hcp-standup). Finally, it is found that the adsorbed H_3C–$C_{(\beta)}{\equiv}C_{(\alpha)(ads)}$ on the bridge site and the top site are ∼0.45 eV and ∼1.01 eV, respectively, higher than that on the hollow sites. These results indicate that the adsorbed H_3C–$C_{(\beta)}{\equiv}C_{(\alpha)(ads)}$ is more likely to locate on the hcpH site rather than to diffuse on the Ag(111) surface.

However, the possible adsorption sites of $H_3C_{(\beta)}C_{(\alpha)}H_2I_{(ads)}$ on the Ag(111) surface after the rupture of the C–I bond still remain unclear. Therefore, several possible adsorption sites of $H_3C_{(\beta)}$–$C_{(\alpha)}H_{2(ads)}$ and $I_{(ads)}$ coadsorbed on the Ag(111) surface are investigated as shown in Figure 2 based on the assumption that the $I_{(ads)}$ will remain on the three-fold hollow site. The corresponding adsorption energies and structure parameters are also summarized in Table I. According to the calculated results, the adsorbed

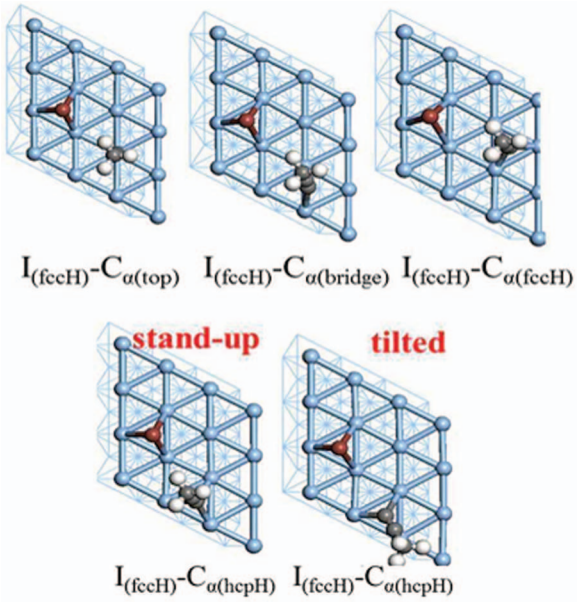

FIG. 1. Some possible optimized structures of H_3C–$C_{(\beta)}{\equiv}C_{(\alpha)(ads)}$ and I coadsorbed on the Ag(111) surface.

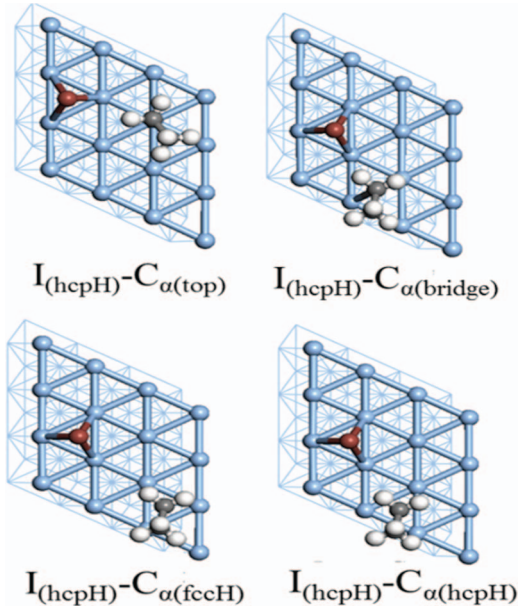

FIG. 2. Some possible optimized structures of $H_3C_{(\beta)}$–$C_{(\alpha)}H_{2(ads)}$ and I coadsorbed on the Ag(111) surface.

$H_3C_{(\beta)}$–$C_{(\alpha)}H_{2(ads)}$ is found to prefer the top site with the adsorption energy of −3.55 eV, namely, the $H_3C_{(\beta)}$–$C_{(\alpha)}H_{2(ads)}$ (top). In addition, the adsorption energy of $H_3C_{(\beta)}$–$C_{(\alpha)}H_{2(ads)}$ on the top site was found to be only ∼0.10 eV lower than the hollow site and ∼0.20 eV lower than the bridge site. As a result, the structural parameters of both C_α–$Ag_{(surface)}$ and C_β–C_α within $H_3C_{(\beta)}$–$C_{(\alpha)}H_{2(ads)}$ adsorbed on the Ag(111) surface are almost the same at different adsorption sites. In other words, the adsorbed $H_3C_{(\beta)}$–$C_{(\alpha)}H_{2(ads)}$ can easily diffuse on the Ag(111) surface because of their similar adsorption energies and adsorption geometries. One thing worth mentioning is that the average adsorption energies of all energetically favorable adsorption sites of H_3C–$C_{(\beta)}\equiv C_{(\alpha)(ads)}$ were found to be ∼2.75 eV lower than that of the adsorbed $H_3C_{(\beta)}$–$C_{(\alpha)}H_{2(ads)}$ on the same surface and their corresponding average C_α–$Ag_{(surface)}$ bond distance of H_3C–$C_{(\beta)}\equiv C_{(\alpha)(ads)}$ was ∼0.741 Å much shorter than that of C_α–$Ag_{(surface)}$ within $H_3C_{(\beta)}$–$C_{(\alpha)}H_{2(ads)}$ adsorbed on the same surface. In the next paragraph, the interfacial electronic properties of both $H_3C_{(\beta)}$–$C_{(\alpha)}H_{2(ads)}$ and H_3C–$C_{(\beta)}\equiv C_{(\alpha)(ads)}$ adsorbed on the Ag(111) surface will be investigated in order to rationalize their different adsorption behaviors between H_3C–$C_{(\beta)}\equiv C_{(\alpha)(ads)}$ and $H_3C_{(\beta)}$–$C_{(\alpha)}H_{2(ads)}$ adsorbed on the Ag(111) surface.

To analyze the interfacial electronic properties between H_3C–$C_{(\beta)}\equiv C_{(\alpha)(ads)}$/ $H_3C_{(\beta)}$–$C_{(\alpha)}H_{2(ads)}$ and the Ag(111) surface, the PDOS projected onto the C_α atom and their neighboring Ag surface atoms for both H_3C–$C_{(\beta)}\equiv C_{(\alpha)(ads)}$ and $H_3C_{(\beta)}$–$C_{(\alpha)}H_{2(ads)}$ adsorbed on the Ag(111) surface are calculated. In addition, the PDOS for both H_3C–$C_{(\beta)}\equiv C_{(\alpha)}$ and $H_3C_{(\beta)}$–$C_{(\alpha)}H_2$ without the effect of Ag(111) surface are also calculated to investigate the interfacial electronic properties upon adsorption. Only two most stable sites are taken into account. The calculated PDOSs are shown in Figures 3 and 4. As shown in the top panels of Figure 3, there are only

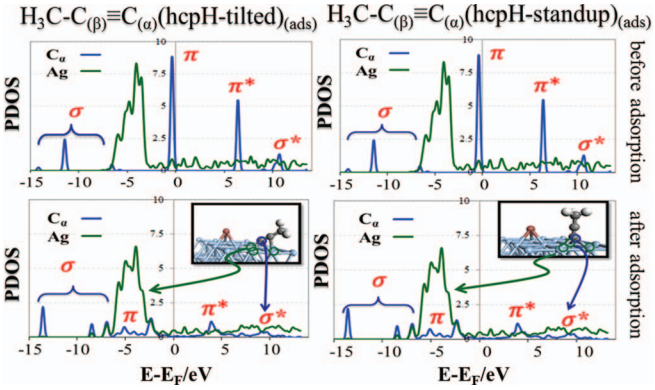

FIG. 3. DOS projected onto the C_α atom (blue line) and Ag *d* states (green line). From left to right: the PDOS of I(hcpH) and H_3C–$C_{(\beta)}\equiv C_{(\alpha)(ads)}$ (hcpH-tilted) coadsorbed on the Ag(111) surface, and I(hcpH) and H_3C–$C_{(\beta)}\equiv C_{(\alpha)(ads)}$ (hcpH-stand up) coadsorbed on the Ag(111) surface. For each system, the top panel shows the PDOS of the isolated subsystems, while the bottom panel refers to the H_3C–$C_{(\beta)}\equiv C_{(\alpha)(ads)}$ after adsorption.

four molecular levels of isolated H_3C–$C_{(\beta)}\equiv C_{(\alpha)(ads)}$, which are identified as σ (−12 eV), π (−1.0 eV), π^* (6.0 eV), and σ^* (11.0 eV) due to their sp hybridization on the C_α atom. The filled d-band of Ag surface can be assigned below the Fermi level in the region from −7.5 eV to −2.5 eV. After adsorption, all the energy peaks of both the C_α state of H_3C–$C_{(\beta)}\equiv C_{(\alpha)(ads)}$ and the filled d-band of Ag surface for two adsorption systems are significantly shifted downward in energy as shown in the bottom panels of Figure 3. The filled d-band of Ag surface is broadened due to two new formed states, which are located at −9.0 eV and −8.0 eV, arising from the overlap of C_α σ state and Ag surface. In addition, the band centered at −5.0 eV and 4.0 eV are identified the π and π^* molecular states and these states spread out significantly to much lower energy levels. Furthermore, the contribution of the π^* orbital near the Fermi level is ascribed to the back-donation of the filled d-band of Ag surface into the empty π^* orbital of the adsorbed H_3C–$C_{(\beta)}\equiv C_{(\alpha)(ads)}$ leading to an increased

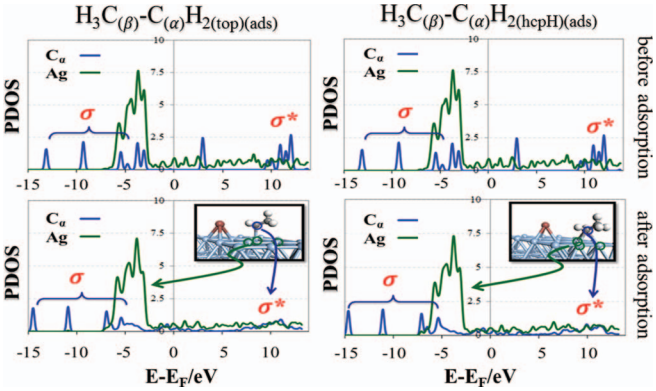

FIG. 4. DOS projected onto the C_α atom (blue line) and Ag *d* states (green line). From left to right: the PDOS of I(hcpH) and $H_3C_{(\beta)}$–$C_{(\alpha)}H_{2(ads)}$(top) coadsorbed on the Ag(111) surface, and I(hcpH) and $H_3C_{(\beta)}$–$C_{(\alpha)}H_{2(ads)}$ (hcpH) coadsorbed on the Ag(111) surface. For each system, the top panel shows the PDOS of the isolated subsystems, while the bottom panel refers to the $H_3C_{(\beta)}$–$C_{(\alpha)}H_{2(ads)}$ after adsorption.

Ag–C bond strength upon adsorption. On the other hand, the calculated PDOS for two most stable adsorption models of $H_3C_{(\beta)}$–$C_{(\alpha)}H_{2(ads)}$ on the Ag(111) surface, that is, $H_3C_{(\beta)}$–$C_{(\alpha)}H_{2(ads)}$(top) and $H_3C_{(\beta)}$–$C_{(\alpha)}H_{2(ads)}$(hcpH), are shown in Figure 4. In the top panels of Figure 4, the C_β–C_α σ states and H–C_α σ states can be assigned at −9.0 eV and the region from the −6.0 eV to −3.0 eV. Those projected σ bonding states are only slightly shifted downwards in energy upon adsorption and the less overlap between the filled d-band of Ag surface and C_α state of $H_3C_{(\beta)}$–$C_{(\alpha)}H_{2(ads)}$ indicates that the Ag–C_α interaction is weak as shown in the bottom panels of Figure 4. In addition, the comparison of the PDOS of $H_3C_{(\beta)}$–$C_{(\alpha)}H_{2(ads)}$ on the top site with that on the hcp hollow site indicates that the $H_3C_{(\beta)}$–$C_{(\alpha)}H_{2(ads)}$ may easily diffuse on the Ag surface because of the similar electronic properties and their weak Ag–C_α interaction. Although these static calculated results can provide us the preliminary understanding for the molecule-substrate interaction upon adsorption, the temperature-dependent adsorption dynamic of both $H_3C_{(\beta)}$–$C_{(\alpha)}H_{2(ads)}$ and H_3C–$C_{(\beta)}\equiv C_{(\alpha)(ads)}$ with $I_{(ads)}$ coadsorbed on the Ag(111) surface still remains unclear. In "IR spectrum of H_3C–$C_{(\beta)}\equiv C_{(\alpha)\,(ads)}$ and $I_{(ads)}$ coadsorbed on the Ag(111) surface at 200 K and 400 K" section, the temperature-dependent infrared (IR) spectrum of these adsorption systems will be calculated based on the DFTMD simulations in combination with a Fourier transform of dipole moment autocorrelation (FT-DMAF). As a byproduct their adsorption dynamics at various temperatures will also be investigated to propose the possible reaction pathways for their self-coupling reactions on the Ag(111) surface.

B. IR spectrum of H_3C–$C_{(\beta)}\equiv C_{(\alpha)\,(ads)}$ and $I_{(ads)}$ coadsorbed on the Ag(111) surface at 200 K and 400 K

As mentioned previously, the rupture of C–I bond within H_3C–$C_{(\beta)}\equiv C_{(\alpha)}I_{(ads)}$ adsorbed on the Ag(111) surface was occurred at 150 K and both H_3C–$C_{(\beta)}\equiv C_{(\alpha)(ads)}$ and $I_{(ads)}$ will be coadsorbed on the Ag(111) surface under the temperature of 500 K based on Chiang's experimental works. Only the thermally most stable configuration of H_3C–$C_{(\beta)}\equiv C_{(\alpha)(ads)}$ and $I_{(ads)}$ coadsorbed on the Ag(111) surface is considered to calculate the IR spectra at 200 K and 400 K using a full DFT Grid charge method for investigating their temperature-dependent dynamic behaviors upon adsorption as shown in Figure 5(a). All of our calculated IR active peaks and experimental RAIRS results are summarized in Table II. The calculated results point out that the IR active peaks of –$C_{(\beta)}\equiv C_{(\alpha)}$– stretching are gradually merged into one peak as the temperature increases from 200 K to 400 K based on their dynamic trajectories of the angle between the –C–$C_{(\beta)}\equiv C_{(\alpha)}$– axis and the Ag(111) surface normal, namely, Ang:[–C–$C_{(\beta)}\equiv C_{(\alpha)}$– axis], at 200 K and 400 K, respectively. The population of Ang:[–C–$C_{(\beta)}\equiv C_{(\alpha)}$– axis] at various temperatures is shown in Figure 5(b). In addition, the calculated maximum population of Ang:[–C–$C_{(\beta)}\equiv C_{(\alpha)}$– axis] at 200 K is found at 35° and 60°, which indicates that there are two orientations of H_3C–$C_{(\beta)}\equiv C_{(\alpha)(ads)}$ adsorbed on the Ag(111) surface, that is, stand-up –$C_{(\beta)}\equiv C_{(\alpha)}$– axis and tilted –$C_{(\beta)}\equiv C_{(\alpha)}$– axis. However, the maximum population of Ang:[–C–$C_{(\beta)}\equiv C_{(\alpha)}$– axis]

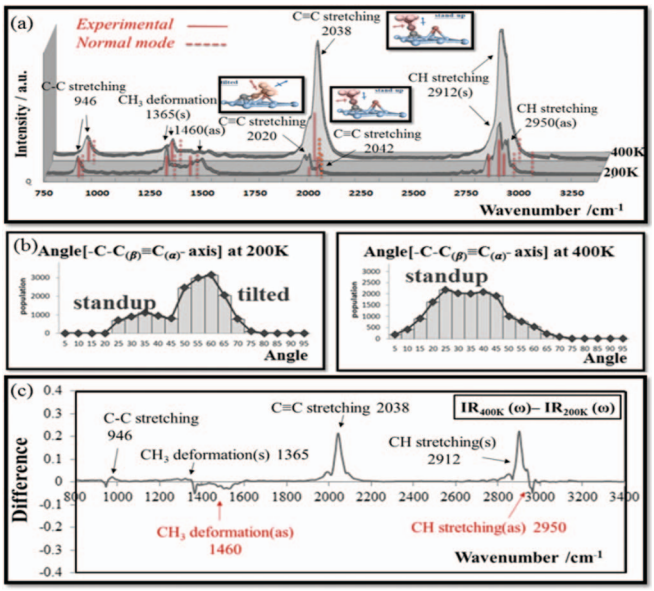

FIG. 5. (a) Calculated IR spectra of H_3C–$C_{(\beta)}\equiv C_{(\alpha)(ads)}$ and $I_{(ads)}$ coadsorbed on the Ag(111) surface at the temperature of 200 K and 400 K, respectively. Experimental and normal mode calculations are included for comparison. (b) The populations of Ang:[–C–$C_{(\beta)}\equiv C_{(\alpha)}$– axis] of H_3C–$C_{(\beta)}\equiv C_{(\alpha)(ads)}$ adsorbed on the Ag(111) surface during DFTMD simulation at 200 K and 400 K, respectively. (c) The temperature difference spectrum of H_3C–$C_{(\beta)}\equiv C_{(\alpha)(ads)}$ and $I_{(ads)}$ coadsorbed on the Ag(111) surface.

is found to be merged into one peak at 30° as temperature increases from 200 K to 400 K, which indicates that there is only one orientation of H_3C–$C_{(\beta)}\equiv C_{(\alpha)(ads)}$ adsorbed on the Ag(111) surface, that is, stand-up –$C_{(\beta)}\equiv C_{(\alpha)}$– axis. Furthermore, the calculated intensities of the IR active peaks of asymmetrical CH_3 deformation mode and asymmetrical CH_3 stretching mode become relatively weak due to the dominant motion of the stand-up –$C_{(\beta)}\equiv C_{(\alpha)}$– axis. To elaborate this feature further the temperature-difference IR spectrum is employed to investigate the intensity change of IR active peaks at various temperatures as shown in Figure 5(c). Evidently, all the IR active peaks can be divided into two groups. The first group includes the bands at 946 cm^{-1} (C–C stretching mode), 2038 cm^{-1} (C≡C stretching mode), and 2912 cm^{-1} (symmetrical CH_3 stretching mode). This group appears at positive side due to the fact that the dominant motion of stand-up –$C_{(\beta)}\equiv C_{(\alpha)}$– axis will increase the intensity of symmetrical modes as temperature increases from 200 K to 400 K. In contrast, the second group includes the bands at 1460 cm^{-1} (asymmetrical CH_3 deformation mode) and 2950 cm^{-1} (asymmetrical CH_3 stretching mode). These peaks appear at negative side due to the same reason that the dominant motion of stand-up –$C_{(\beta)}\equiv C_{(\alpha)}$– axis will decrease the intensity of asymmetrical modes. Indeed, as expected, the IR spectra of the H_3C–$C_{(\beta)}\equiv C_{(\alpha)(ads)}$ and $I_{(ads)}$ coadsorbed on the Ag(111) surface will have the temperature-dependent behavior because of obvious changes for the population of the orientation of the adsorbed H_3C–$C_{(\beta)}\equiv C_{(\alpha)(ads)}$ as temperature increases from 200 K to 400 K.

TABLE II. Calculated major IR active peaks of both $H_3C–C_{(\beta)}{\equiv}C_{(\alpha)(ads)}$ and $H_3C_{(\beta)}–C_{(\alpha)}H_{2(ads)}$ with $I_{(ads)}$ coadsorbed on the Ag(111) surface at various temperatures upon adsorption. Experimental RAIRS and calculated normal mode IR peaks (without scaling factor of 0.9612) are also included for comparison.

$H_3C–C{\equiv}C_{(ads)}$ and $I_{(ads)}$ coadsorbed on Ag(111)	Normal mode (0 K)	Chiang's work exp. (200 K)	MD-this work (200 K)	Chiang's work exp. (200 K)	MD-this work (400 K)
υC–C stretching	965	944	946	946	965
ρCH_3 rocking	1063	N.A.	N.A.	N.A.	N.A.
δCH_3 deformation (s)	1442	1367	1365	1369	1365
δCH_3 deformation (as)	1503	1425	1460	N.A.	N.A.
υC≡C stretching	2130	2020;2042	2020;2042	2038	2038
υCH_3 stretching (s)	3027	2904	2912	2912	2904
υCH_3 stretching (as)	3108	2956	2950	N.A.	N.A.
$H_3CCH_{2(ads)}$ and $I_{(ads)}$ coadsorbed on Ag(111)	Normal mode (0K)	White's work expt. (100K)	MD-this work (100K)	White's work expt. (150K)	MD-this work (150K)
υC–C stretching	943	930	910	920	910
ωCH_2 bending	1069	1100	1094	1100	1091
ωCH_2 wagging	1194	1194	1201	1197	1201
δCH_3 deformation (s)	1388	1374	1370	1374	1370
δCH_3 deformation (as)	1484	1433	1469	1433	1469
υCH_3 stretching (s)	2894	2914	2909	2904	2909
υCH_2 stretching (s)	2961	2944	2950	2944	2950
υCH_3 stretching (as)	3039	2974	2970	2964	2970
υCH_2 stretching (as)	3108	3002	3012	3002	3012

C. IR spectrum of $H_3C_{(\beta)}–C_{(\alpha)}H_{2(ads)}$ and $I_{(ads)}$ coadsorbed on the Ag(111) surface at 100 K and 150 K

By comparing with the $H_3C–C_{(\beta)}{\equiv}C_{(\alpha)}I_{(ads)}$ molecule, the dissociation reaction of the C–I bond within $H_3C_{(\beta)}–C_{(\alpha)}H_2I_{(ads)}$ adsorbed on the Ag(111) surface will occur at much lower temperature of 110 K and both $H_3C_{(\beta)}–C_{(\alpha)}H_{2(ads)}$ and $I_{(ads)}$ will be stably coadsorbed on the Ag(111) surface under 200 K. Only the thermally most stable configuration of $H_3C_{(\beta)}–C_{(\alpha)}H_{2(ads)}$ and $I_{(ads)}$ coadsorbed on the Ag(111) surface is considered to calculate the IR spectra at temperature of 100 K and 150 K, respectively, for investigating their temperature-dependent dynamic behaviors upon adsorption as shown in Figure 6(a). The calculated IR peaks between 2850 and 3050 cm^{-1} are attributed to the C–H stretching. Due to different hybridization of the carbon atom ($C_{(\alpha)sp2}$ vs. $C_{(\beta)sp3}$), the corresponding IR frequencies of $C_{(\alpha)sp2}$–H stretching should be higher than the $C_{(\beta)sp3}$–H stretching. Hence, the IR signature of the C–H stretching of $H_3C_{(\beta)}–C_{(\alpha)}H_{2(ads)}$ can be assigned into four peaks as follows: 2909 cm^{-1}, 2970 cm^{-1} (symmetrical and asymmetrical of $C_{(\beta)sp3}$–H stretching mode), 2950 cm^{-1}, and 3012 cm^{-1} (symmetrical and asymmetrical of $C_{(\alpha)sp2}$–H stretching mode). The IR active peaks at 1370 cm^{-1} and 1469 cm^{-1} are attributed to the symmetrical CH_3 deformation and asymmetrical CH_3 deformation. The IR active peaks at 1201 cm^{-1} and 1094 cm^{-1} correspond to the CH_2 wagging and CH_2 bending. Finally, the IR active peak at 910 cm^{-1} is assigned to the $C_{(\beta)}–C_{(\alpha)}$ stretching. Indeed, all calculated IR active peaks are in a good agreement with White's experimental RAIRS data as summarized in Table II. To elaborate the effect of temperature on the IR active peaks, the same strategy is employed to calculate the difference of the IR spectrum of $H_3C_{(\beta)}–C_{(\alpha)}H_{2(ads)}$ and $I_{(ads)}$ coadsorbed on the Ag(111) between 100 K and 150 K as shown in Figure 6(c). The calculated results indicate that most IR active peaks remain unchanged except for a slight increase of the CH_2 bending and the symmetrical CH_3 stretching as temperature increases from 100 K to 150 K. In order to explain the relationship between the orientation of the adsorbed $H_3C_{(\beta)}–C_{(\alpha)}H_{2(ads)}$ and their corresponding IR active peaks, the population of the angle between the $–C_{(\beta)}–C_{(\alpha)}–$ axis and the Ag(111) surface normal, namely, Ang:[-–$C_{(\beta)}–C_{(\alpha)}–$ axis], is analyzed during DFTMD simulation at 100 K and 150 K, respectively. The calculated maximum population of Ang:[$–C_{(\beta)}–C_{(\alpha)}–$ axis] at 100 K and 150 K are found to be 65° and 60°, respectively, as shown in Figure 6(b). In other

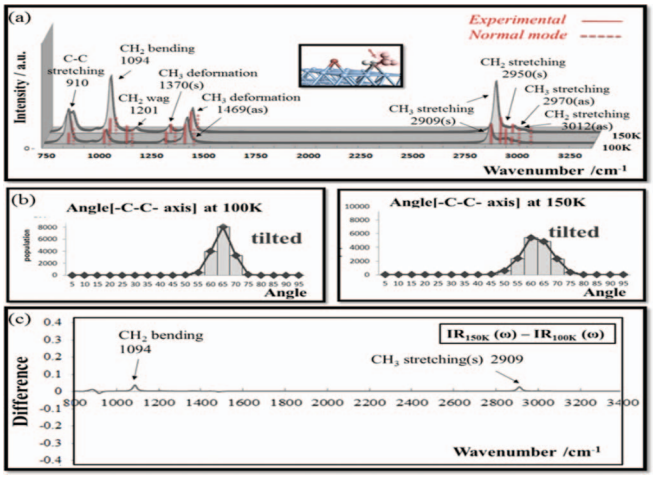

FIG. 6. (a) Calculated IR spectra of $H_3C_{(\beta)}–C_{(\alpha)}H_{2(ads)}$ and $I_{(ads)}$ coadsorbed on the Ag(111) surface at the temperature of 100 K and 150 K. Experimental and normal mode calculations are included for comparison. (b) The populations of Ang:[$–C_{(\beta)}–C_{(\alpha)}–$ axis] of $H_3C_{(\beta)}–C_{(\alpha)}H_{2(ads)}$ adsorbed on the Ag(111) surface during DFTMD simulation at 100 K and 150 K, respectively. (c) The temperature difference spectrum of $H_3C_{(\beta)}–C_{(\alpha)}H_{2(ads)}$ and $I_{(ads)}$ coadsorbed on the Ag(111) surface.

words, as the temperature increases from 100 K to 150 K, the orientation of the adsorbed $H_3C_{(\beta)}$–$C_{(\alpha)}H_{2(ads)}$ still remains the tilted –$C_{(\beta)}$–$C_{(\alpha)}$– axis and the maximum population of Ang:[–$C_{(\beta)}$–$C_{(\alpha)}$– axis] only slightly decreases 5°. These observations lead to the conclusion that the dominant motion of the adsorbed $H_3C_{(\beta)}$–$C_{(\alpha)}H_{2(ads)}$, which is less temperature-dependent, causes the presence of the asymmetrical IR active peaks, such as the asymmetrical CH_3 deformation and the asymmetrical of CH_2/CH_3 stretching, in the calculated IR spectra as the temperature increases from 100 K to 150 K.

Based on calculated results of both H_3C–$C_{(\beta)}\equiv C_{(\alpha)(ads)}$ and $H_3C_{(\beta)}$–$C_{(\alpha)}H_{2(ads)}$ on the Ag(111) surface, different kinds of dynamic behaviors of these two adsorbents are observed. Two orientations of the adsorbed H_3C–$C_{(\beta)}\equiv C_{(\alpha)(ads)}$, that is, the tilted –$C_{(\beta)}\equiv C_{(\alpha)}$– axis and stand-up –$C_{(\beta)}\equiv C_{(\alpha)}$– axis were observed at 200 K in comparison with only one orientation of the adsorbed $H_3C_{(\beta)}$–$C_{(\alpha)}H_{2(ads)}$, that is, tilted –$C_{(\beta)}$–$C_{(\alpha)}$– axis was observed at 100 K. As the temperature increases, H_3C–$C_{(\beta)}\equiv C_{(\alpha)(ads)}$ is found to be stably adsorbed on the most favorable adsorption site (three-fold hollow) even at the temperature of 400 K but the population of Ang:[–$C_{(\beta)}\equiv C_{(\alpha)}$–axis] is significantly changed. These observations imply that a flipping energy of the adsorbed H_3C–$C_{(\beta)}\equiv C_{(\alpha)(ads)}$ from the tilted –$C_{(\beta)}\equiv C_{(\alpha)}$– axis to the stand-up –$C_{(\beta)}\equiv C_{(\alpha)}$– axis is required due to the thermally less stable geometry of the stand-up –$C_{(\beta)}\equiv C_{(\alpha)}$– axis. On the other hand, as the temperature increases, the adsorbed $H_3C_{(\beta)}$–$C_{(\alpha)}H_{2(ads)}$ is found to slightly diffuse on the Ag(111) surface even at the temperature of 150 K. In addition, the tilted motion of the –$C_{(\beta)}$–$C_{(\alpha)}$– axis of $H_3C_{(\beta)}$–$C_{(\alpha)}H_{2(ads)}$ remains unchanged. Apparently, these different kinds of dynamic behavior of H_3C-$0C_{(\beta)}\equiv C_{(\alpha)(ads)}$ and $H_3C_{(\beta)}$-$0C_{(\alpha)}H_{2(ads)}$ adsorbed on the Ag(111) surface might have strong influence on their temperature-dependent diffusion processes on the same surface. Therefore, it is essential to examine the effect of the temperature on their diffusion processes in order to provide further insights into the factors governing C_α–C_α self-coupling reaction of H_3C–$C_{(\beta)}\equiv C_{(\alpha)(ads)}$ and $H_3C_{(\beta)}$–$C_{(\alpha)}H_{2(ads)}$ on the Ag(111) surface. In "Diffusion of H_3C–$C_{(\beta)}\equiv C_{(\alpha)\,(ads)}$ and $H_3C_{(\beta)}$–$C_{(\alpha)}H_{2(ads)}$ with I coadsorbed on the Ag(111) surface" section, the DFTMD simulations of these adsorption systems at higher temperatures will be performed to investigate their possible diffusion pathways on the Ag(111) surface.

D. Diffusion of H_3C–$C_{(\beta)}\equiv C_{(\alpha)\,(ads)}$ and $H_3C_{(\beta)}$–$C_{(\alpha)}H_{2(ads)}$ with I coadsorbed on the Ag(111) surface

To appreciate the effect of temperature on the diffusion dynamics of both H_3C–$C_{(\beta)}\equiv C_{(\alpha)(ads)}$ and $H_3C_{(\beta)}$–$C_{(\alpha)}H_{2(ads)}$ with $I_{(ads)}$ coadsorbed on the Ag(111) surface, firstly, it is realized that C_α–C_α self-coupling reaction of H_3C–$C_{(\beta)}\equiv C_{(\alpha)(ads)}$ and $H_3C_{(\beta)}$–$C_{(\alpha)}H_{2(ads)}$ on the Ag(111) surface is experimentally observed at 500 K and 200 K, respectively, through TPRS results. Secondly, it would be possible to observe the diffusion process of both H_3C–$C_{(\beta)}\equiv C_{(\alpha)(ads)}$ on the Ag(111) surface from 200 K up to 500 K and $H_3C_{(\beta)}$–$C_{(\alpha)}H_{2(ads)}$ on the Ag(111) surface from 100 K up to 200 K. Therefore, during the 8.0 ps dynamic runs, the position of C_α atom of both H_3C–$C_{(\beta)}\equiv C_{(\alpha)(ads)}$ and $H_3C_{(\beta)}$–$C_{(\alpha)}H_{2(ads)}$ will be traced within the range of temperature mentioned above in order to investigate their possible diffusion pathways. The xy-projections of the collected dynamic trajectories of the position of C_α atom of H_3C–$C_{(\beta)}\equiv C_{(\alpha)(ads)}$ and $I_{(ads)}$ at temperatures (200 K, 400 K, and 500 K) are shown in Figure 7(a). On the basis of these dynamic trajectories, the most possible diffusion pathways can be easily established. For example, both H_3C–$C_{(\beta)}\equiv C_{(\alpha)(ads)}$ and $I_{(ads)}$ were found to be stably located on the three-fold hollow site at 200 K and 400 K. As the temperature increases to 500 K, the adsorbed H_3C–$C_{(\beta)}\equiv C_{(\alpha)(ads)}$ start to diffuse from a three-fold hollow site to another three-fold hollow site across the bridge site. However, $I_{(ads)}$ still locates at the three-fold hollow, which exhibited the less dependency on the dynamic motion of H_3C–$C_{(\beta)}\equiv C_{(\alpha)(ads)}$ adsorbed on the Ag(111) surface, even at the temperature of 500 K. This significantly higher temperature to prompt the diffusion process from the most stable site (three-fold hollow site) to the metastable site (bridge site) is due to the strong Ag–C_{sp} bond as discussed previously. On the other hand, the xy-projections of the collected dynamic trajectories of the position of C_α atom of $H_3C_{(\beta)}$–$C_{(\alpha)}H_{2(ads)}$ and $I_{(ads)}$ during the entire DFTMD simulations at various temperatures (100 K, 150 K, and 200K) are shown in Figure 7(b). According to the dynamic results, the adsorbed $H_3C_{(\beta)}$–$C_{(\alpha)}H_{2(ads)}$ was found to slightly diffuse around the top site at low temperature (T = 150 K) due to the very weak Ag–C_{sp3} bond. As the temperature increases to 200 K, the adsorbed $H_3C_{(\beta)}$–$C_{(\alpha)}H_{2(ads)}$ start to diffuse toward different sites on the Ag(111) surface. Following these observed trajectories, two most possible diffusion pathways can be easily established as shown in Figure 7(b) (Nose thermostat: 200 K). First, the $H_3C_{(\beta)}$–$C_{(\alpha)}H_{2(ads)}$ diffuses from top site to another top site across a bridge site. Then, the $H_3C_{(\beta)}$–$C_{(\alpha)}H_{2(ads)}$ diffuses from the three-fold hollow site to another three-fold hollow site across a bridge site. Again, $I_{(ads)}$ was also found to be less dependent on the dynamic motion of the adsorbed $H_3C_{(\beta)}$–$C_{(\alpha)}H_{2(ads)}$ as the temperature increases from 100 K to 200 K.

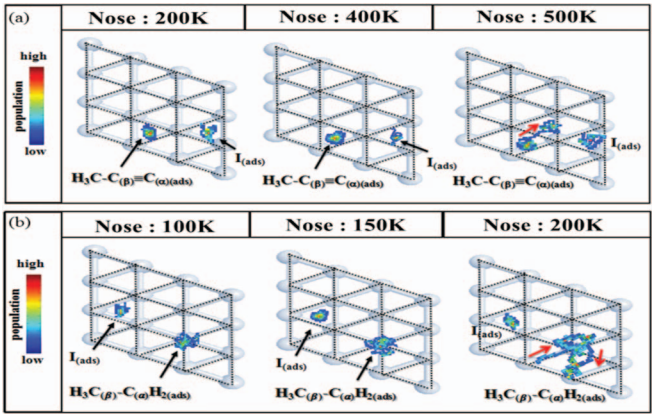

FIG. 7. (a) The population of both H_3C–$C_{(\beta)}\equiv C_{(\alpha)(ads)}$ and $I_{(ads)}$ projected onto the Ag(111) surface during the DFTMD simulations at 200 K, 400 K, 500 K. (b) The population of both $H_3C_{(\beta)}$–$C_{(\alpha)}H_{2(ads)}$ and $I_{(ads)}$ projected on the Ag(111) surface during the DFTMD simulations at 100 K, 150 K, and 200 K.

Throughout these collected dynamic trajectories, the diffusion processes of $H_3C–C_{(\beta)}\equiv C_{(\alpha)(ads)}$ and $H_3C_{(\beta)}–C_{(\alpha)}H_{2(ads)}$ can be easily observed on the Ag(111) surface at 500 K and 200 K, respectively. Furthermore, the diffusion is the elementary step to initiate the $C_\alpha–C_\alpha$ self-coupling reaction. Therefore, it is essential to investigate the reaction pathways of the $C_\alpha–C_\alpha$ self-coupling reaction by taking these diffusion processes into account. In "Self-coupling reaction of both $H_3C–C_{(\beta)}\equiv C_{(\alpha)\,(ads)}$ and $H_3C_{(\beta)}–C_{(\alpha)}H_{2(ads)}$ on the Ag(111) surface" section, the thermally favorable reaction pathways for $C_\alpha–C_\alpha$ self-coupling reaction of both $H_3C–C_{(\beta)}\equiv C_{(\alpha)(ads)}$ and $H_3C_{(\beta)}–C_{(\alpha)}H_{2(ads)}$ adsorbed on the Ag(111) surface and their corresponding transition state structures will be further investigated.

E. Self-coupling reaction of both $H_3C–C_{(\beta)}\equiv C_{(\alpha)\,(ads)}$ and $H_3C_{(\beta)}–C_{(\alpha)}H_{2(ads)}$ on the Ag(111) surface

Based on previous diffusion results, the diffusion trajectories of both $H_3C–C_{(\beta)}\equiv C_{(\alpha)(ads)}$ and $H_3C_{(\beta)}–C_{(\alpha)}H_{2(ads)}$ on the Ag(111) surface can be further applied to establish the reaction pathways for $C_\alpha–C_\alpha$ self-coupling leading to the formation of 2,4-hexadiyne ($H_3C–C\equiv C–C\equiv C–CH_{3(g)}$) and butane ($CH_3–CH_2–CH_2–CH_{3(g)}$). We have proposed several reaction pathways to calculate their corresponding reaction barrier for the Cα–Cα self-coupling reaction of H3C–C(β)≡C(α)(ads) and H3C(β)–C(α)H2(ads) on the Ag(111) surface (see supplementary material[44]). In order to locate their transition-state structures for $C_\alpha–C_\alpha$ self-coupling of both $H_3C–C_{(\beta)}\equiv C_{(\alpha)(ads)}$ and $H_3C_{(\beta)}–C_{(\alpha)}H_{2(ads)}$ on the Ag(111) surface along our proposed reaction pathways, the PSCPM is used and the calculated energy barriers will be corrected by the ZPE. Additionally, a minima structure (no imaginary frequency) and a transition state (one and only one imaginary normal mode frequency) are verified. Figures 8 and 9 show the overall energetic profiles for $C_\alpha–C_\alpha$ self-coupling of both $H_3C–C_{(\beta)}\equiv C_{(\alpha)(ads)}$ and $H_3C_{(\beta)}–C_{(\alpha)}H_{2(ads)}$ on the Ag(111) surface. Based on the calculated results, it is found that the energy barrier for $C_\alpha–C_\alpha$ self-coupling reaction of $H_3C_{(\beta)}–C_{(\alpha)}H_{2(ads)}$ to form $H_3C–C\equiv C–C\equiv C–CH_{3(g)}$ along the hollow-bridge-hollow reaction pathway on the Ag(111) surface is 1.34 eV, which is 0.74 eV higher than that of $H_3C_{(\beta)}–C_{(\alpha)}H_{2(ads)}$ to form $CH_3–CH_2–CH_2–CH_{3(g)}$ along the similar reaction pathway. On the other hand, the calculated energy barrier for $C_\alpha–C_\alpha$ self-coupling reaction of $H_3C_{(\beta)}–C_{(\alpha)}H_{2(ads)}$ along the top-bridge-top reaction pathway is found to be ∼0.32 eV, a little bit higher than that of $H_3C_{(\beta)}–C_{(\alpha)}H_{2(ads)}$ along the hollow-bridge-hollow reaction pathway as shown in Figure 9. In addition, the total energy of initial state (IS) along the hollow-bridge-hollow reaction pathway is found to be 0.03 eV lower than that along the top-bridge-top reaction pathway. Based on these calculated results, the reaction pathway along the hollow-bridge-hollow can be referred to the most favorable reaction pathway. To realize the effect of molecular geometry on their different energy barrier for $C_\alpha–C_\alpha$ self-coupling, the detailed structural parameters are reported in Table III. By comparing with the structures of $H_3C–C_{(\beta)}\equiv C_{(\alpha)(ads)}$ and $H_3C_{(\beta)}–C_{(\alpha)}H_{2(ads)}$ from the reactant to the transition, it can be observed that (1) the large distortion of Ang:[$–C_{(\beta)}\equiv C_{(\alpha)}–$ axis] of $H_3C–C_{(\beta)}\equiv C_{(\alpha)(ads)}$ is found (from 3.7° to 60.0°) and (2) the adsorbed $H_3C–C_{(\beta)}\equiv C_{(\alpha)(ads)}$ remain closely to the Ag(111) surface ($Ag_{suf}–C_\alpha$: from 1.485 Å to 1.620 Å) than $H_3C_{(\beta)}–C_{(\alpha)}H_{2(ads)}$ ($Ag_{suf}–C_\alpha$: from 2.115 Å to 2.624 Å) on the same surface along the reaction pathway. These results pointed out that much more energy for the adsorbed $H_3C–C_{(\beta)}\equiv C_{(\alpha)(ads)}$ is required to weaken the Ag–C interaction leading to the transition state structure with a higher activation energy barrier for $C_\alpha–C_\alpha$ self-coupling reaction. The calculated activation energy barrier for the coupling reaction of both $H_3C–C_{(\beta)}\equiv C_{(\alpha)(ads)}$ and $H_3C_{(\beta)}–C_{(\alpha)}H_{2(ads)}$ (1.34 eV and 0.60 eV) on the Ag(111) surface is qualitatively agreeable with the trend of reaction temperatures of the experimental TPRS observations (∼500 K and ∼200 K).

To further validate our proposed reaction pathways, the second-order Polanyi-Wigner equation and Redhead Approximation are employed to realize the relationship between the experimental reaction temperatures and calculated activation energy barrier. Based on second-order Polanyi-Wigner equation as described earlier, the maximum desorption temperature for the $C_\alpha–C_\alpha$ self-coupling reaction can be predicted by using the following parameters: (1) the energy barrier for the desorption process, ΔE, which can be determined by investigating the overall desorption process and the energy barrier for the $C_\alpha–C_\alpha$ self-coupling reaction within the thermally most favorable diffusion process of both $H_3C–C_{(\beta)}\equiv C_{(\alpha)(ads)}$ and $H_3C_{(\beta)}–C_{(\alpha)}H_{2(ads)}$ on the Ag(111) surface (the coupling

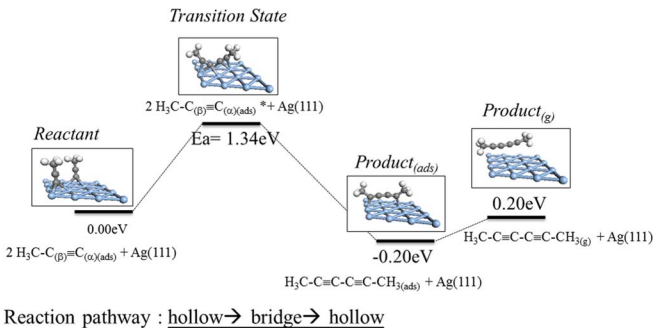

FIG. 8. The possible energetic profile for self-coupling reaction of $H_3C–C_{(\beta)}\equiv C_{(\alpha)(ads)}$ coadsorbed on the Ag(111) surface along the hollow-bridge-hollow reaction pathway.

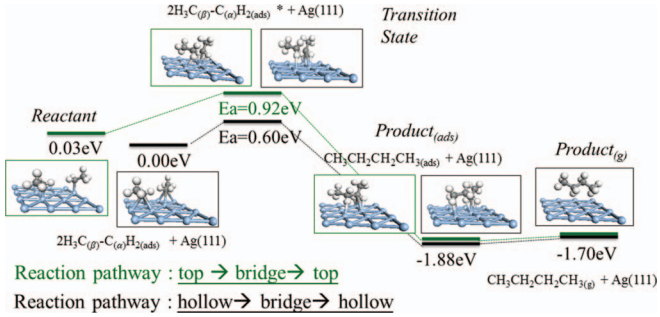

FIG. 9. Two possible energetic profiles for self-coupling reaction of $H_3C_{(\beta)}–C_{(\alpha)}H_{2(ads)}$ coadsorbed on the Ag(111) surface along the top-bridge-top reaction pathway (green line) and the hollow-bridge-hollow reaction pathway (black line).

TABLE III. Calculated bond lengths (Å) of the reactant, transition state, and product (a) along (a) the hollow-bridge-hollow reaction pathway for self-coupling reaction of $H_3C–C_{(\beta)}{\equiv}C_{(\alpha)(ads)}$ coadsorbed on the Ag(111) surface and (b) the hollow-bridge-hollow reaction pathway for self-coupling reaction of $H_3C_{(\beta)}–C_{(\alpha)}H_{2(ads)}$ coadsorbed on the Ag(111) surface.

$H_3CC{\equiv}C_{(ads)}$ self-coupling on Ag(111)	Reactant	TS	Product	Ea	Redhead approximation temp.
$C_{\alpha(sp)}–C_{\alpha(sp)}$ (Å)	4.431	1.884	1.381	1.34eV	510 K (expt. 515 K)
Ave[$Ag_{(surface)}$– C_α] (Å)	1.485	1.620	2.311		
Ave[$Ag_{(surface)}$- C_β] (Å)	2.700	2.245	2.211		
Ave[$C_\alpha{\equiv}C_\beta$]	1.252	1.286	1.301		
Ang[–$C_\alpha{\equiv}C_\beta$– axis]	3.7°	60°	97.2°		
$H_3CCH_{2(ads)}$ self-coupling on Ag(111)	Reactant	TS	Product	Ea	Redhead approximation temp.
$C_{\alpha(sp3)}–C_{\alpha(sp3)}$ (Å)	4.342	2.271	1.530	0.60 eV	230 K (expt. 200 K)
Ave[$Ag_{(surface)}$- C_α] (Å)	2.115	2.624	3.352		
Ave[$Ag_{(surface)}$- C_β] (Å)	2.813	3.451	2.970		
Ave[C_α–C_β]	1.527	1.502	1.525		
Ang[–C_α–C_β– axis]	63.0°	75.9°	79.1°		

barrier: 1.34 eV and 0.60 eV) are considered rather than their desorption energies (the desorption barrier: 0.40 eV and 0.17 eV) due to the rate-determinate step; (2) the pre-exponent factor, v, which is estimated by extracting the vibrational frequency of molecule and substrate during DFTMD simulations and the calculated frequency of the Ag–C bond is found to be around 300 cm^{-1} (0.9×10^{13} s^{-1}) similar to the experiment that commonly used (10^{12}–10^{13} s^{-1}); (3) the heating rate, $_\beta$, which is 2 K/s consistent with the experimental data; and (4) the surface coverage of our proposed adsorption models of both $H_3C–C_{(\beta)}{\equiv}C_{(\alpha)(ads)}$ and $H_3C_{(\beta)}–C_{(\alpha)}H_{2(ads)}$ on the Ag(111) surface, *N*, which are low-coverage adsorption (2/9 ML). Following these mentioned parameters the calculated reaction temperatures for the C_α–C_α self-coupling reaction of both $H_3C–C_{(\beta)}{\equiv}C_{(\alpha)(ads)}$ and $H_3C_{(\beta)}–C_{(\alpha)}H_{2(ads)}$ on the Ag(111) surface are 510 K and 230 K, respectively. To further discuss the relationship between our calculated results and the experimental ones, the following experimental observations are worth to mention. The experimental reaction temperatures of both the $H_3C–C_{(\beta)}{\equiv}C_{(\alpha)(ads)}$ and $H_3C_{(\beta)}–C_{(\alpha)}H_{2(ads)}$ on the Ag(111) surface are decreased as the surface coverage increases from low-coverage to high-coverage adsorption (510 K to 470 K and 200 K to 180 K) due to fact that the desorption temperature is a function of the surface coverage for a second-order coupling reaction. Indeed, our predicted reaction temperatures for the coupling reaction of both $H_3C–C_{(\beta)}{\equiv}C_{(\alpha)(ads)}$ and $H_3C_{(\beta)}–C_{(\alpha)}H_{2(ads)}$ are found to be much closer to the low-coverage TPRS results (515 K and 200 K) as expected.

IV. CONCLUSIONS

By combining DFTMD simulations with FT-DMAF, the simulated IR spectra of both $H_3C–C_{(\beta)}{\equiv}C_{(\alpha)(ads)}$ and $H_3C_{(\beta)}–C_{(\alpha)}H_{2(ads)}$ adsorbed on the Ag(111) surface are provided in order to compare with the experimental RAIRS results. In addition, DFTMD simulations also allow us to investigate the effect of temperature on their adsorption dynamics. Based on collected dynamic trajectories of adsorbed molecules, the thermally induced diffusion processes of both $H_3C–C_{(\beta)}{\equiv}C_{(\alpha)(ads)}$ and $H_3C_{(\beta)}–C_{(\alpha)}H_{2(ads)}$ adsorbed on the Ag(111) surface are used to establish the most probable reaction pathways for the self-coupling reaction of both $H_3C–C_{(\beta)}{\equiv}C_{(\alpha)(ads)}$ and $H_3C_{(\beta)}–C_{(\alpha)}H_{2(ads)}$ adsorbed on the Ag(111) surface. Furthermore, the activation energy barriers for these thermally most possible reaction pathways can be converted into the reaction temperatures through the second-order Redhead approximation. The calculated reaction temperatures are in a good agreement with the low-coverage experimental TPRS data. Finally, it is our hope that this study will stimulate more experimental works to provide more dynamic and microscopic pictures of organic compounds adsorbed on the metal surfaces leading to the coupling products in order to have a better understanding of heterogeneous catalytic reactions.

ACKNOWLEDGMENTS

The authors would like to thank the National Council in Taiwan for financial support (Grant Nos. NSC 97-2113-M-032-003-MY3 and NSC 100-2113-M-032-002) and the National Center for High Performance Computing and Tamkang University in Taiwan for the use of computational facilities.

[1]J. L. Lin and B. E. Bent, J. Am. Chem. Soc. **115**, 6943 (1993).
[2]X. L. Zho and J. M. White, J. Phys. Chem. **95**, 5575 (1991).
[3]C. M. Chiang, T. H. Wentzlaff, and B. E. Bent, J. Phys. Chem. **96**, 1836 (1992).
[4]H. J. Wu, H. K. Hus, and C. M. Chiang, J. Am. Chem. Soc. **121**, 4433 (1999).
[5]P. Chuang, Y. L. Chan, S. H. Chien, R. Klauser, and T. J. Chuang, Chem. Phys. Lett. **354**, 179 (2002).
[6]Q. Y. Yang, K. J. Maynard, A. D. Johnson, and S. T. Ceyer, J. Chem. Phys. **102**, 7734 (1995).
[7]H. Kung, S. M. Wu, Y. J. Wu, Y. W. Yang, and C. M. Chiang, J. Am. Chem. Soc. **130**, 10263 (2008).
[8]R. B. Anderson, *The Fischer-Tropsch Synthesis* (Academic Press, New York, 1984).
[9]N. Sheppard and C. D. L. Cruz, Adv. Catal. **41**, 1 (1996).
[10]N. Sheppard and C. D. L. Cruz, Adv. Catal. **42**, 181 (1998).
[11]H. Kung, L. C. Lee, S. M. Wu, H. Y. Cheng, and C. M. Chiang, J. Am. Chem. Soc. **129**, 1028 (2007).
[12]X. L. Zhou and J. M. White, Catal. Lett. **6**, 375 (1989).
[13]W. Huang and J. M. White, J. Am. Chem. Soc. **126**, 14527 (2004).

[14]M. F. Mrozek, M. J. Weaver, J. Phys. Chem. B **105**, 8931 (2001).
[15]K. Itoh, T. Kiyohara, H. Shinohara, C. Ohe, Y. Kawamura, and H. Nakai, J. Phys. Chem. B **106**, 10714 (2002).
[16]A. Kokalj, A. D. Corso, S. de Gironcoli, and S. Baroni, J. Phys. Chem. B **106**, 9839 (2002).
[17]W. X. Huang and J. M. White, J. Phys. Chem. B **108**, 7911 (2004).
[18]Z. P. Liu and P. Hu, J. Am. Chem. Soc. **124**, 11568 (2002).
[19]J. Cheng, P. Hu, P. Ellis, S. French, G. Kelly, and C. M. Lok, J. Phys. Chem. C **112**, 6082 (2008).
[20]J. Chen and Z. P. Liu, J. Am. Chem. Soc. **130**, 7929 (2008).
[21]T. E. Shubina, C. Hartnig, and M. T. M. Koper, Phys. Chem. Chem. Phys. **6**, 4215 (2004).
[22]T. A. Baker, B. Xu, X. Liu, E. Kaxiras, and C. M. Friend, J. Phys. Chem. C **113**, 16561 (2009).
[23]S. Izvekov, A. Mazzolo, K. VanOpdorp, and G. A. Voth, J. Chem. Phys. **114**, 3248 (2001).
[24]S. Izvekov and G. A. Voth, J. Chem. Phys. **115**, 7196 (2001).
[25]S. Meng, E. G. Wang and S. Gao, Phys. Rev. B **69**, 195404 (2004).
[26]M. Konôpka, I. Ŝtich, and K. Terakura, Phys. Rev. B **65**, 125418 (2002).
[27]J. S. Lin, S. Y. Lu, P. J. Tseng, and W. C. Chou, J. Comput. Chem. **33**, 1274 (2012).
[28]J. M. Soler, E. Artacho, J. D. Gale, A. Garcia, J. Junquera, P. Ordejón, and D. Sánchez-Portal, J. Phys. Condens. Matter **14**, 2745 (2002).
[29]N. Troullier and J. L. Martins, Phys. Rev. B **43**, 1993 (1991).
[30]J. P. Perdew, K. Burke, and M. Ernzerhof, Phys. Rev. Lett. **77**, 3865 (1996).
[31]J. S. Lin and W. C. Chou, J. Phys. Chem. C **112**, 768 (2008).
[32]H. J. Monkhorst and J. D. Pack, Phys. Rev. B **13**, 5188 (1976).
[33]R. N. Barnett and U. Landman, Phys. Rev. B **48**, 2081 (1993).
[34]S. Nosé, J. Chem. Phys. **81**, 511 (1984).
[35]W. G. Hoover, Phys. Rev. A **31**, 1695 (1985).
[36]M. P. Gaigeot, R. Vuilleumier, M. Sprik, and D. Borgis, J. Chem. Theory Comput. **1**, 772 (2005).
[37]P. h. Berens and K. R. Wilson, J. Chem. Phys. **74**, 4872 (1981).
[38]M. A. Czarnecki, P. Wu, and H. W. Siesler, Chem. Phys. Lett. **283**, 326 (1998).
[39]J. S. Lin and Y. T. Kuo, Thin Solid Films **370**, 192 (2000).
[40]J. S. Lin and L. F. Lee, Quantum Chem. **97**, 736 (2004).
[41]D. A. King, Surf. Sci. **47**, 384 (1975).
[42]A. M. de Jong and J. W. Niemantsverdriet, Surf. Sci. **233**, 355 (1990).
[43]P. A. Redhead, Vaccum **12**, 203 (1962).
[44]See supplementary material at http://dx.doi.org/10.1063/1.4861036 for the proposed reaction pathways.